# Cs diffusion mechanisms in UO_2 investigated by SIMS, TEM, and atomistic simulations

C. Panetier, Y. Pipon, C. Gaillard, D. Mangin, J. Amodeo, J. Morthomas, T. Wiss, A. Benedetti, R. Ducher, R. Dubourg, et al.

# Cs diffusion mechanisms in $UO_2$ investigated by SIMS, TEM and atomistic simulations

C. Panetier[a], Y. Pipon[a,b*], C. Gaillard[a], D. Mangin[c], J. Amodeo[d,e], J. Morthomas[d], T. Wiss[f], A. Benedetti[f], R. Ducher[g], R. Dubourg[g], N. Moncoffre[a]

[a] Univ Lyon, Univ Claude Bernard Lyon 1, CNRS/IN2P3, IP2I Lyon, UMR 5822, F-69622, Villeurbanne, France

[b] Univ Lyon, UCBL, IUT Lyon-1, Département chimie, F-69622, Lyon, France

[c] IJL, Université de Lorraine, CNRS : UMR7198 – CS 14234 54042 Nancy Cedex, France

[d] Univ Lyon, INSA Lyon, UCBL, CNRS, MATEIS, UMR5510, 69621 Villeurbanne, France

[e] Aix Marseille Univ., Université de Toulon, CNRS, IM2NP, Marseille, France

f European Commission, DG Joint Research Centre, Directorate G –Nuclear Safety and Security, PO box 2340, D-76125 Karlsruhe, Germany

[g] IRSN, LETR – BP3 13115 St-Paul-Lez-Durance Cedex, France

*** Corresponding author:** Yves PIPON

E-mail: y.pipon@ipnl.in2p3.fr

Postal address: Université de Lyon, UCBL, IP2I, Campus LyonTech La Doua, 4 rue Enrico Fermi, 69622 Villeurbanne cedex, France

## Highlights

New insights on Cs diffusion mechanisms in $UO_2$ derived from atomistic calculations obtained with semi-empirical potentials and supported by SIMS and TEM experimental data.

Keywords: $UO_2$, Cs, diffusion, SIMS, MD, TEM

## ABSTRACT

Experimental investigations and atomistic simulations are combined to study the cesium diffusion processes at high temperature in $UO_2$. After $^{133}Cs$ implantation in $UO_2$ samples, diffusion coefficients are determined using the depth profile evolution after annealing as measured by secondary ion mass spectrometry. An activation energy of 1.8 ± 0.2 eV is subsequently deduced in the 1300-1600°C temperature range. Experimental results are compared to nudged elastic band simulations performed for different atomic paths including several types of uranium vacancy defects. Activation energies ranging from 0.49 up to 2.34 eV are derived, showing the influence of the defect (both in terms of type and concentration) on the Cs diffusion process. Finally, molecular dynamics simulations are performed, allowing the identification of preferential Cs trajectories that corroborate experimental observations.

# 1. INTRODUCTION

After major nuclear accidents (e.g., Chernobyl 1986, Fukushima Daichii 2011), large quantities of $^{137}Cs$, a highly radiotoxic element with a half-life of 30 years, were disseminated outside the nuclear power plants with catastrophic consequences for the environment [1]. Hence, it is essential to improve our knowledge about the behaviour of this fission product (FP) present in nuclear fuels to better anticipate the implications of such events. To tackle this problem, several international research programs such as VERCORS, VEGA or VERDON [2–6] have focused on the FP behaviour in irradiated nuclear fuels (mainly $UO_2$) in order to investigate several accidental scenarios (including atmosphere and temperature variations). As a main output, after an initial cesium release at 1500°C, a strong release was measured when the nuclear fuel was subjected to high temperatures (above 2000-2300°C), confirming the volatile nature of cesium. Nevertheless, only few information about the underlying migration mechanisms are available due to the complexity of the parameters involved, which include variations in atmosphere composition, temperature, burnup and number of defects.

On the other hand, literature data show that Cs diffusion coefficients were exclusively determined from post-irradiation annealing release measurements using the Booth model [7] which is an indirect way to calculate apparent diffusion coefficients including among others the effect of extended defects and other fission product contributions. These diffusion coefficients were fitted using an Arrhenius law, giving access to activation energies (Ea) and pre-exponential factors ($D_0$) ranging from 1.6 eV to 4.3 eV and from 2.1 $10^{-8}$ $cm^2$ $s^{-1}$ and 3.4 $10^{-2}$ $cm^2$ $s^{-1}$, respectively, within the 1450 – 2500°C temperature range [5,8]. Such high discrepancies can be explained by the differences in irradiation history between all the experiments. Therefore, in order to get better insights on the diffusion mechanisms, the role of defects created during irradiation has to be assessed.

For this purpose, several authors performed atomistic simulations to provide inputs about Cs incorporation and mobility at various positions within the $UO_2$ unit cell [9–12]. These studies show that cesium is favourably incorporated in uranium vacancies ($V_U$), sole or in clusters of defects that contain oxygen vacancies ($V_O$) such as the divacancy ($V_U + V_O$), the Schottky defects ($V_U + 2V_O$) or the tetravacancy ($2V_U + 2V_O$). Furthermore, Gupta *et al.* determined Cs and U migration energy barriers between uranium vacancies in the <110> direction using the nudged elastic band (NEB) method and obtained activation energies of 2.72 eV and 5.6 eV, respectively [9,13]. Hence, these studies emphasized that uranium diffusion is the rate limiting process that controls the Cs diffusion in $UO_2$. However, these NEB simulations represented a simplified first approach, ignoring complex pathways and other major defects such as Schottky defects. Therefore, the present study proposes new insights on the Cs thermal behaviour in $UO_2$ coupling direct experimental observations and atomistic

calculations. It aims at determining Cs diffusion mechanisms and associated kinetics considering the major point defects (single vacancies, divacancies and Schottky defect) associated to the $UO_2$ lattice. For this purpose, ion implantation is used to introduce cesium in $UO_2$ pellets which are further annealed at temperatures representative of normal and accidental conditions in a light water reactor (LWR) fuel i.e., in the 1000°C to 1600°C temperature range. Cesium depth profiles are measured by secondary ion mass spectrometry (SIMS), both before and after annealing. Diffusion coefficients of cesium in $UO_2$ are then determined from the depth profile evolution in the 1300-1600°C temperature range. In parallel, atomistic calculations using empirical potentials are performed to identify the elementary diffusion processes. First, Cs migration energies in $UO_2$ are calculated for predetermined atomic trajectories associated to different defects in the crystal using the NEB method. Then, molecular dynamic (MD) outcomes allow to identify preferential elementary jump processes of Cs diffusion at high temperature.

# 2. METHODS

## 2.1 Experimental procedure

We used depleted $UO_2$ pellets (0.2 at.% of $^{235}U$), provided by the Framatome company and sintered at 1750°C under a reducing atmosphere (5% $H_2$/Ar) during 5 h. This procedure guarantees an O/U ratio of 2.00 ± 0.01 and a high bulk density (97.5% of the theoretical density). The average grain size is 11 µm, which is comparable to that of the LWR nuclear fuel. Pellets were polished on one side by the PRIMEVerre society (Montpellier, France) with diamond paste and then annealed twice. To degas adsorbed particles on the surface, samples were first annealed in a PECKLY© tubular furnace at 1000°C during 10 h under vacuum ($10^{-7}$ mbar). Then, a second annealing, at 1600°C for 4 h in a NABERTHERM© tubular furnace was performed under a 5%$H_2$/Ar gas mixture flowing through ultra-high capacity oxygen and moisture filters. These conditions allow to anneal defects induced by the polishing and to maintain the $UO_{2.00}$ stoichiometry.

Next, pellets were implanted under vacuum ($P < 5.10^{-6}$ mbar) with 800 keV $^{133}Cs^{2+}$ ions at a fluence of $10^{15}$ Cs $cm^{-2}$. A cooling device was used to maintain the sample temperature at 15°C in order to prevent any oxidation.

The Cs distribution and the displacements per atom (dpa) as a function of the implantation depth were computed using the SRIM software [14]. Threshold displacements values of U and O atoms were put at 40 eV and 20 eV respectively [15] and the code was run using the full cascade mode. Figure 1 shows a Cs profile corresponding to an implantation fluence of $10^{15}$ at $cm^{-2}$. It shows a quasi-Gaussian distribution centred at a mean projected range (Rp) of 140 nm with a maximum Cs concentration of 0.08 at.%. The maximum number of 9 dpa at a depth of 80 nm indicates a high damage level in the

material. This value is only indicative as the SRIM code does not account for the material annealing occurring even at room temperature after each displacement cascade. As shown in a previous experimental work using Transmission Electron Microscopy (TEM) [16], these implantation conditions lead to the formation of two damaged regions. The first one, between the surface and about 85 nm from it, contains mainly point defects whereas the second one, that extends down to around 200 nm, shows mainly irradiation-induced dislocation loops.

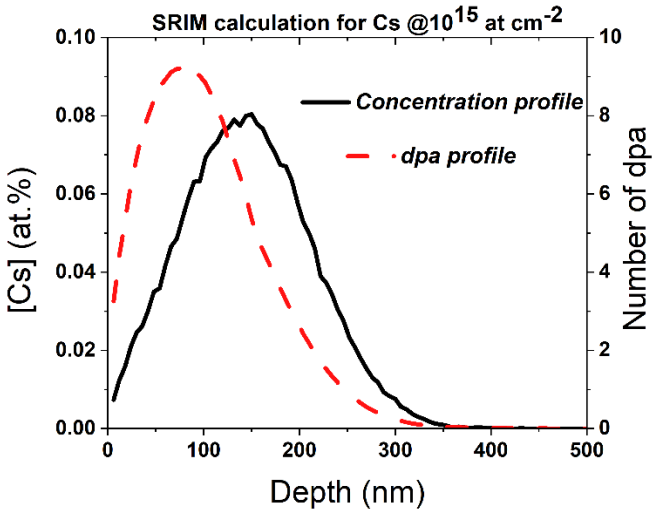


**Figure 1-** SRIM calculations of Cs concentration profile and number of dpa with respect to depth for a Cs implantation energy of 800 keV and a fluence of $10^{15}$ Cs $cm^{-2}$.

After implantation, pellets were annealed at different temperatures between 1000°C and 1600°C in a 5% $H_2$/Ar atmosphere to promote Cs migration in stoichiometric $UO_2$. Cs depth profiles were measured by SIMS before and after annealing on a CAMECA IMS 7f facility equipped with an eucentric rotating sample stage designed by CAMECA to inhibit the surface roughening of poly-crystalline materials. Its velocity was set to 8 rpm for each analysis. A primary beam of 10 keV $O_2^+$ ions was used to sputter the $UO_2$ sample surface creating 250 × 250 µm² rasters. Secondary ions ($^{238}U^{16}O^+$ and $^{133}Cs^+$) were collected on the raster central part (62 µm diameter) to avoid wall effects. At least three craters were made for each SIMS analysis and three depth profiles (later averaged) were consequently obtained. More details about the experimental procedure and the data processing based on the relative sensitivity factor (RSF) can be found in [16].

Microstructural observations were also done at the JRC (Joint Research Centre) Karlsruhe, Germany. First, a FEI™ VERSA 3D Focused Ion Beam (FIB), was used to prepare electron transparent lamellae from the $UO_2$ samples. Samples were covered with a sputtered 40-50 nm gold layer and then a double platinum layer was deposited in the FIB, using the electron beam first and the ion beam then, to protect the surface during milling operations. Once the Pt deposit was made, two trenches were cut with the $Ga^+$ ion beam, then the remaining lamella was cut free from the sample, removed with an Omniprobe

needle and attached to a Cu grid. Thinning and final cleaning of the lamella were then performed at decreasing voltages, taking extreme care not to consume the protecting layer and to avoid introducing artefacts in the sample. The final thickness of the lamella varied between 30-60 nm. TEM analysis were then performed with a 200 keV electron beam on a Tecnai G2 TEM FEI microscope. Both Bright Field (BF) and High Resolution (HR) images were recorded at different sample areas, as well as energy dispersive X-ray spectra.

## 2.2 Simulation method

### 2.2.1 Interatomic potentials and simulation parameters

Molecular statics (MS) and dynamics as well as NEB simulations were performed using the rigid ion (RI) model (cf. equation 1) parameterised by Grimes and Catlow to study the stability of several FPs in $UO_2$ [11]. To our knowledge, this is the only potential available in literature that includes cesium interactions with oxygen and uranium. In this model, pair interactions are calculated using long-range Coulombic interactions ($q_i$ and $q_j$ are the charges of the two ions) and a short-range Buckingham term. A cut-off radius of 10.4 Å was set for all short-range interactions as done in [17]. Long-range Coulombic interactions were computed using the Ewald summation [18]. All potential parameters are provided in Table 1.

$$V_{ij}(\mathrm{r}_{ij}) = \frac{q_i q_j}{4\pi\varepsilon_0 r} + A_{ij} e^{-\frac{r}{\rho_{ij}}} - \frac{C_{ij}}{r^6} \qquad (equation\ 1)$$

**Table 1-** Grimes and Catlow parametrization for $UO_2$ and Cs interatomic potentials [11].

| | $U^{4+}$-$U^{4+}$ | $U^{4+}$-$O^{2-}$ | $O^{2-}$-$O^{2-}$ | $Cs^{+}$-$U^{4+}$ | $Cs^{+}$-$O^{2-}$ |
|---|---|---|---|---|---|
| **$A_{ij}$ (eV)** | 18600 | 2494.20 | 108.00 | 18659.60 | 649.60 |
| **$\rho_{ij}$ (Å)** | 0.27468 | 0.34123 | 0.38000 | 0.29505 | 0.41421 |
| **$C_{ij}$ (eV Å$^{-6}$)** | 32.64 | 40.16 | 56.06 | 48.62 | 64.34 |

Additional static simulations were performed using the core-shell (CS) model provided by Grimes and Catlow [11] that allows for polarizability effects. In this model, each atom is modelled by a core linked to its electronic shell by a harmonic spring, the net charge of the atom being computed as the sum of both contributions (core and shell). In this case, the short-range interactions are computed from shell interactions only. All the parameters used for the CS model can be found in [11]. The LAMMPS [19] code is used for both the RI and CS models.

### 2.2.2 Static calculations of intrinsic defect formation energy in $UO_2$

The formation energy of neutral intrinsic defects in $UO_2$, i.e. Frenkel pairs and Schottky defects, were calculated using classical energy minimization of the system with and without the defect. Simulations were done using a 5 x 5 x 5 fluorite unit supercell (1500 atoms) and tri-periodic boundary conditions (PBC). This system size is large enough to constrain the influence of the replica while keeping reasonable cpu costs (see [17] for more details). Minimizations were achieved with the conjugate gradient algorithm using a force norm of $10^{-10}$ eV.Å$^{-1}$ as a stopping criterion.

Using LAMMPS, the Frenkel pair formation energies were determined by calculating the energy difference between the defective lattice and the perfect one. For the Schottky defect, the formation energy relies on the cohesive energy of a $UO_2$ molecule to account for the number of atom variation. In addition to LAMMPS simulations, we used the Mott-Littleton approach implemented in GULP [20] to compare our results with those of Govers *et al.* [17]. The spheres radii within the Mott-Littleton approach were set to 9 and 20 Å respectively in accordance with [17].

### 2.2.3 NEB calculations of Cs and U migration

The Climbing Image (CI-) NEB method [21] is used to compute diffusion minimum energy paths (MEPs) of U and Cs atoms along the <100> and <110> directions in $UO_2$. The system contains 1500 atoms and the simulations are performed using PBCs. The initial NEB path is made out of 17 interpolated replicas and is relaxed using the FIRE 2.0 damped dynamics minimizer [22,23] and a timestep of 0.1 ps. We chose the parallel nudging force to be based on interpolated ideal position and the perpendicular nudging force was computed to improve calculation convergence. The values of the parallel and perpendicular nudging forces between the replicas were both set to 5.0 eV Å$^{-1}$. The stopping criterion of the simulation was set to a force tolerance of 0.01 eV Å$^{-1}$.

### 2.2.4 MD simulation of Cs diffusion in $UO_2$

The simulation temperature was fixed at 2227°C to improve Cs mobility statistics while being in the temperature range used in the literature experiments [5]. All MD simulations were performed using a timestep of 1 fs. First, the system is heated to the target temperature using a rate of 100°C/ps before being equilibrated for 50 ps in the NPT ensemble. Nosé-Hoover thermostat and barostat are used with relaxation times of 0.1 ps and 5.0 ps, respectively.

After equilibration, the mean square displacements (MSD) of each element (Cs, U, O) was computed in the NVE ensemble for a total time ($N_t$) of 200 ps using equation 2.

$$\langle \Delta r(t)^2 \rangle = \frac{1}{NN_t} \sum_{i=1}^{N} \sum_{t=t_0}^{N_t} \left( r_i(t + t_0) - r_i(t_0) \right)^2 \qquad (equation\ 2)$$

Where: $r_i(t)$ is the position of the $i^{th}$ atom at time t ($t_0$ being the beginning of the simulation), N is the total number of considered atoms and $N_t$ is the MSD calculation total time.

# 3. RESULTS

## 3.1 Cesium thermal migration in $UO_2$: experimental results

Figure 2 shows the cesium concentration distributions obtained by SIMS in $UO_2$ samples implanted at a fluence of $10^{15}$ Cs $cm^{-2}$ after annealing between 1000 and 1600°C. They have been determined from the average roughness of SIMS craters (horizontal error bars) and from the RSF uncertainty (vertical error bars).

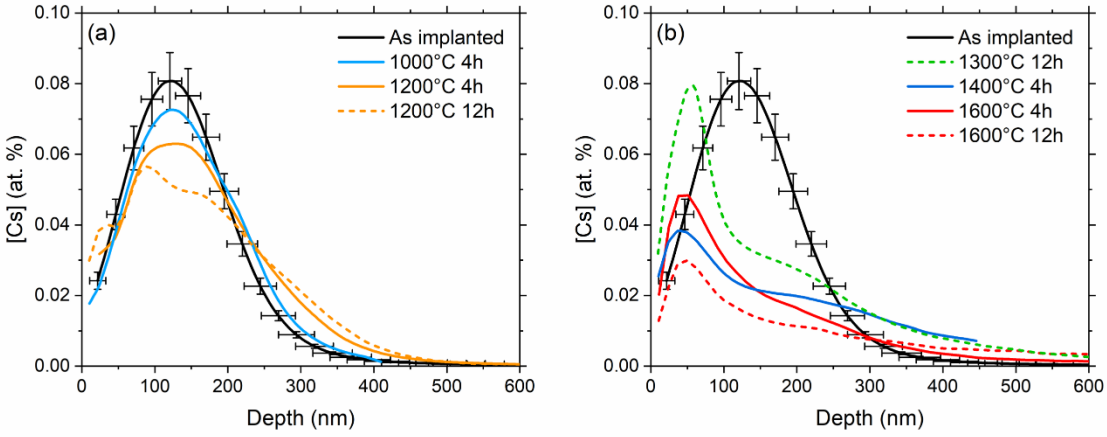


**Figure 2-** Cs depth profiles in $UO_2$ samples implanted at $10^{15}$ Cs $cm^{-2}$ annealed under reducing atmosphere between 1000 and 1200°C (a) and between 1300 and 1600°C (b). The as-implanted sample's profile is the reference. Continuous lines are for 4h annealing and dashed ones for 12h annealing. Error bars have been added only on the as-implanted profiles in order to distinguish all depth profiles.

Figure 2(a) shows no significant Cs diffusion (nor release) in $UO_2$ annealed at 1000°C (within the error bars). In contrast, profiles after annealing at 1200°C are significantly different even if no release was measured. Indeed, after four hours of annealing, the tail of the distribution (beyond 250 nm) is larger and the maximum concentration is lower. After twelve hours, the evolution of the Cs distribution is noteworthy as three maxima appear at around 30, 90 and 170 nm. This indicates the beginning of Cs migration processes (diffusion, trapping, …) that change with depth, Cs local concentration and defect local concentration. The profile evolution initially observed at 1200°C seems to stabilize for temperatures larger than 1300°C where the depth profiles exhibit the same three peaks shape (see

225 Figure 2(b)) but centred at different depths. At 1200°C, there is a first Cs peak at 50 nm from the
226 surface, followed by a shoulder around 100 nm and a contribution at depths superior to 400 nm
227 (beyond the end of the as-implanted profile), corresponding to Cs thermal diffusion. We note that no
228 apparent release occurred at 1300°C (within the error bars). However, starting from 1400°C, significant
229 release can be calculated: 40%, 35% and 48% for the 1400°C-4h, 1600°C-4h and 1600°C-12h annealing
230 respectively[1]. To sum up, the non-steady state Cs diffusion occurs with the same mechanisms between
231 1300°C and 1600°C but differs at 1200°C that is rather characterized by a transient regime. Therefore,
232 no diffusion coefficient was determined at 1200°C in this study.
233 In order to determine the Cs diffusion coefficients in $UO_2$ at 1300, 1400 and 1600°C, each depth profile
234 was first fitted using Gaussian curves. An example of a fit achieved on the Cs depth distribution
235 measured after the 1600°C-12h annealing is presented in Figure 3. The fit with G1, G2 and G3 (Gaussian
236 contributions) was done enforcing a maximum deviation of 5 nm for the maximum position of each
237 Gaussian curve (respectively 50 nm from the surface, 140 nm and 100 nm), therefore restricting the
238 total number of solutions to a few ones very close to each other.
239 The physical meaning of each contribution can be extrapolated from the work of Hocking *et al.* who
240 used SIMS to profile iodine in polycrystalline $UO_2$ samples implanted with $^{127}I$ at 900 keV at a fluence
241 of $10^{13}$ at $cm^{-2}$ [24]. After annealing (between 1200 and 1650°C), Hocking *et al.* observed little evolution
242 of the profile part corresponding to iodine concentrations above $10^{16}$ at $cm^{-3}$ (~0.1 at.ppm). This was
243 explained by iodine trapping in irradiation induced defects. Below this concentration threshold, in the
244 tail of the profiles, iodine thermal (atomic) diffusion was highlighted. In our work, the G1 curve
245 represents the Cs atoms trapped into faceted and spherical bubbles (see e.g., [16]) at 50 nm from the
246 surface. The second Gaussian distribution (G3) accounts for the Cs atoms trapped into the vacancies
247 created during implantation at around 100 nm, near the maximum of dpa calculated by SRIM (see
248 Figure 1). There is also a possibility that these Cs atoms are trapped into nanobubbles not visible by
249 microscopy with a size inferior to 1 nm. The third contribution (G2) is attributed to Cs thermal diffusion,
250 since it was detected up to a depth of 800 nm in a zone free from implantation defects. We have
251 chosen to centre it at a depth corresponding to the Rp (140 nm) of the as-implanted depth profile.
252 Hence, this last contribution (G2) was used to determine the Cs diffusion coefficients.

[1] The 1400°C-4h distribution does not take into account the totality of the Cs in the sample as the SIMS analysis was stopped too early, thus leading to a probable overestimation of the Cs release from this sample but without changing the distribution shape and its straggling.

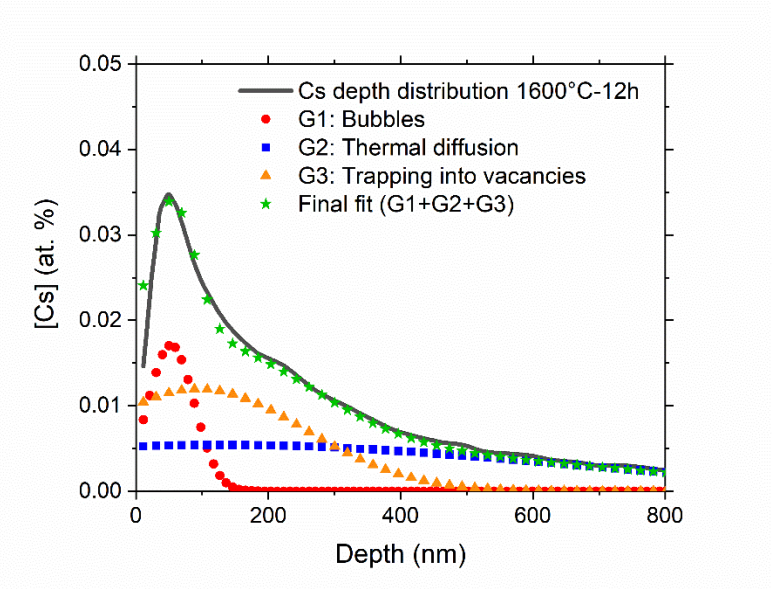


**Figure 3-** Fit of the Cs depth profile obtained after annealing at 1600°C-12h. The three Gaussian curves (G1, G2 and G3) represent Cs bubble formation, thermal diffusion and trapping into vacancies, respectively. The sum of the three contributions fits the experimental curve.

Apparent diffusion coefficients *D* were determined using the Fick's second law as one of its analytical solution is a Gaussian curve with standard deviation (noted $\sigma_f$ or $\sigma_i$) proportional to $\sqrt{2Dt}$. Considering that both the initial (as-implanted) and final state of the Cs (annealed sample) are fitted with Gaussian curves, we can thus deduce Cs diffusion coefficient using equation 3.

$$D\ (cm^2\ s^{-1}) = \frac{\sigma_f^2 - \sigma_i^2}{2t} \qquad \text{(equation 3)}$$

Values are reported in Table 2. Errors were determined from the uncertainty on the standard deviation of the G2 curve and were calculated with the lowest and highest standard deviation values obtained from each fit.

**Table 2-** Cs apparent diffusion coefficients and release fraction in $UO_2$ at 1300, 1400 and 1600°C. *The Cs release fraction is overestimated due to the fact that the concentration profile was not measured up to the end.

| Annealing conditions | $D_{Cs}$ ($10^{-14}$ cm² $s^{-1}$) | Cs release fraction |
|---|---|---|
| 1300°C-12h | 0.8 ± 0.2 | 0 % |
| 1400°C-4h | 2.2 ± 1.3 | 40 %* |
| 1600°C-4h | 8.5 ± 3.8 | 35 % |
| 1600°C-12h | 4.6 ± 3.7 | 48 % |

The temperature dependence of Cs diffusion in $UO_2$ is retrieved from the Arrhenius diagram presented in Figure 4 using a linear fit. Results lead to an activation energy of 1.8 ± 0.2 eV and a pre-exponential factor equal to (8.4 ± 5.6) × $10^{-9}$ $cm^2$ $s^{-1}$ for the Cs diffusion in $UO_2$.

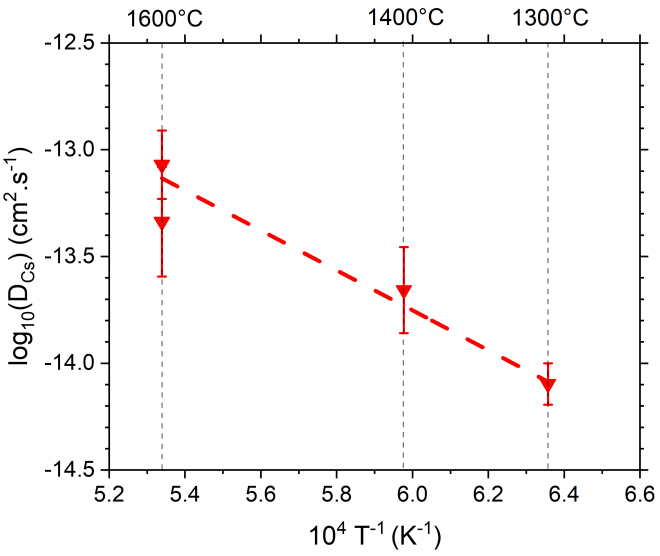


**Figure 4-** Arrhenius plot showing the temperature dependence of Cs diffusion coefficients in $UO_2$

## 3.2 Microstructure of the $UO_2$ sample annealed at 1200°C-12h

The Cs profiles determined from the samples annealed at 1200°C (4h and 12h) display a transition between the profile of the sample annealed at 1000°C (no variation with resepect to the as implanted sample) and the profiles of the samples annealed at 1300°C, 1400°C and 1600°C (which all exhibit a similar trend). Therefore, it was of particular interest to perform TEM analysis on the sample annealed at 1200°C – 12h. Figure 5 displays three zones which can be delimited at ~80 nm and ~150 nm from the surface. Zone 3 corresponds to the region free (or almost free) of implantation defects and some features (circled in yellow) can be seen near the zone 2 / zone 3 interface. The zone 1 / zone 2 interface corresponds to the maximum of the dpa profile as calculated by SRIM (see Figure 1).

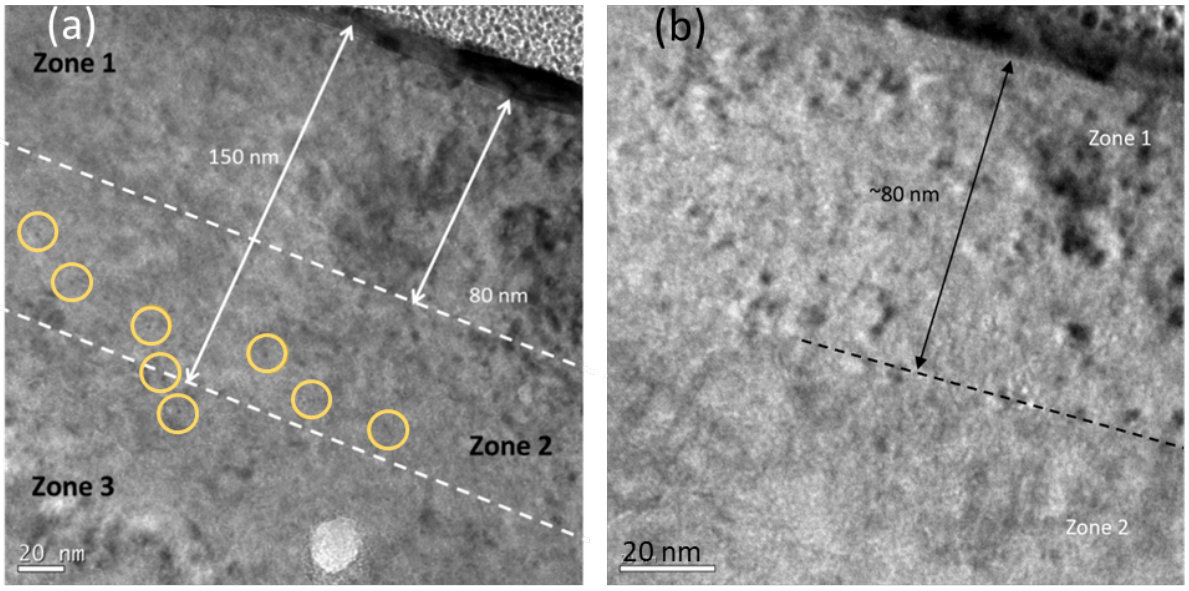


**Figure 5-** TEM image of the $UO_2$ sample implanted with cesium and annealed at 1200°C-12h. (a) illustration of the three different zones. (b) zoom at the zone 1 / zone 2 frontier. Yellow circles highlight features attributed to large bubbles.

At higher magnification, small features within zone 1 become visible. These features can be highlighted by acquiring over focused and under focused images of the same region, as shown in Figure 6. It can be seen that the contrast of each feature is inverted (from black to white or vice versa) when passing through focus, unlike what happens for strain contours. This clearly indicates presence of nanobubbles. Their exact size is not measurable due to the defocus, but it is certainly below 1 nm in agreement with what was recently observed by Onofri *et al.* [25]. Density values for the nanobubbles would be very difficult to calculate, due to their extremely small size as well as to the masking effect of the strain contours. Nevertheless, a very rough estimate based on the counting of visible bubbles in Figure 6, and considering an average thickness of 30 nm (based on the visibility of lattice fringes) would lead to a bubble density of the order of magnitude of $10^{24}$ bubbles $m^{-3}$.

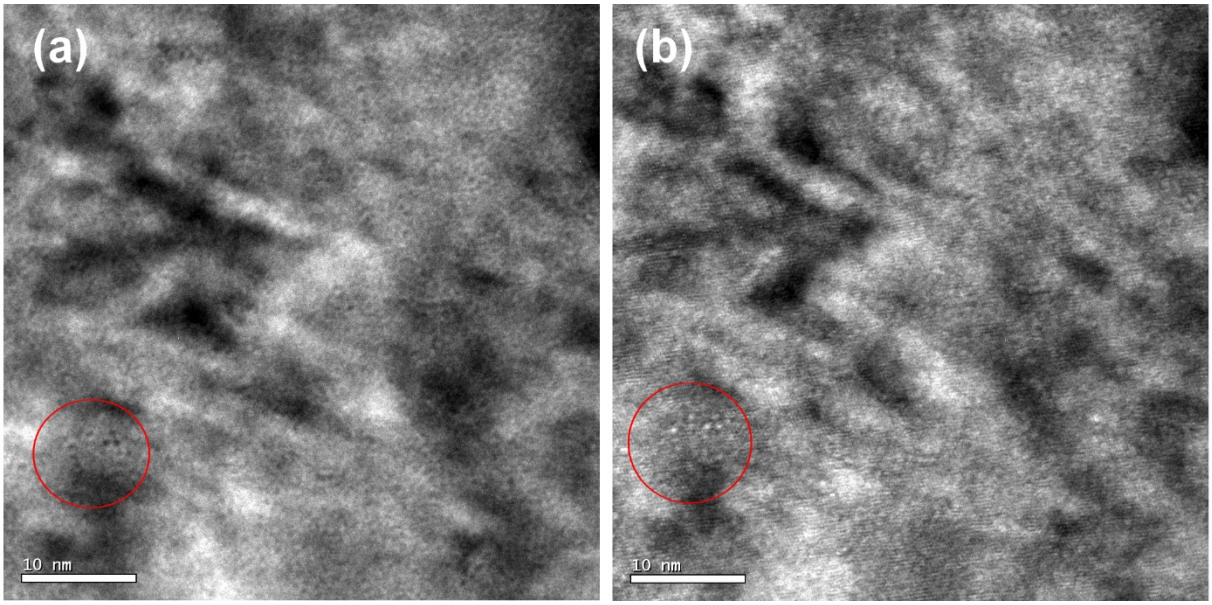


**Figure 6-** TEM image of the $UO_2$ sample implanted with cesium and annealed at 1200°C-12h in zone 1 in under-focus (a) and over-focus (b) conditions. Red circle highlights the presence of several nanobubbles

In zone 2 and zone 3, these nanobubbles are also present. Moreover, some bigger bubbles can be observed especially at a depth of around 160 nm from the surface (interface zone 2 / zone 3) where most of dislocations are present. The presence of dislocation segments is in agreement with what was found by He *et al.* on Kr-implanted $UO_2$ for similar damage levels [26]. Figure 7 presents a TEM image at the zone 2 / zone 3 interface showing such larger (~5 nm) bubbles. Some rare faceted bubbles around 5 nm in size can be also observed in Figure 7 (yellow circle).

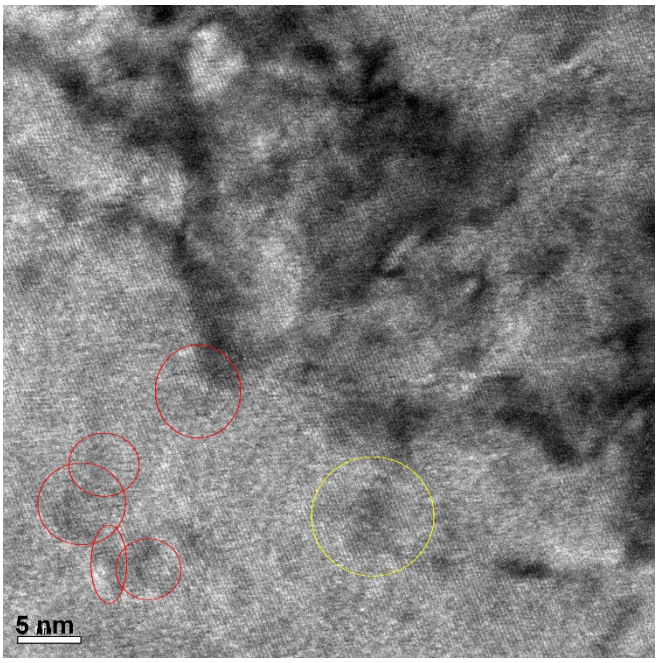


**Figure 7-** HREM image at a depth of 160 nm from the surface of an $UO_2$ sample implanted with cesium and annealed at 1200°C-12h. In red, nanobubbles and in yellow, faceted bubble

The smaller, spherical nanobubbles, ~1 nm in size, can be observed until a depth of around 300 nm from the surface. These results are to be compared with those obtained at 1600°C in a previous study [16] where no bubbles were observed apart in a restricted area near the surface. They confirm that 1200°C seems to be a threshold temperature in the migration of cesium in $UO_2$.

## 3.3 Simulation results

### 3.3.1 $UO_2$ intrinsic defect formation energies at 0K

$UO_2$ intrinsic defect formation energies (DFE) are presented in Table 3 where they are compared to DFT [27,28] and additional MS calculations performed by Sattonnay and Tetot [29] using the variable charge SMTB-Q interatomic potential. Two kind of defects were created: Frenkel Pairs (one vacancy and one interstitial far from each other) of oxygen or uranium and Schottky defects (one uranium vacancy and two oxygen vacancies).

**Table 3-** DFE (eV) of intrinsic neutral defects in $UO_2$ calculated with Grimes potential with the rigid ion (RI) model and the core shell (CS) model, using LAMMPS and GULP codes. FP = Frenkel Pairs. S = Schottky defects. Three possible configurations exist to place the oxygen vacancies around the uranium vacancy in the <100> (S1), <110> (S2) or <111> (S3) direction.

| Model | **This work** | | | CS model *GULP* **[17]** | SMTB-Q **[29]** | DFT **[27,28]** |
|---|---|---|---|---|---|---|
| | RI model *LAMMPS* | CS model *LAMMPS* | CS model *GULP* | | | |
| **$FP_O$** | 7.8 | 7.0 | 5.8 | 5.8 | 4.4 | 5.3 |
| **$FP_U$** | 28.2 | 24.8 | 18.9 | 18.9 | 6.1 | 15.8 |
| **S1** | 8.9 | 8.1 | 7.3 | 7.3 | 5.9 | 10.7 |
| **S2** | 9.2 | 8.4 | 7.0 | 7.0 | 5.9 | |
| **S3** | 10.5 | 9.5 | 7.2 | 7.2 | 6.4 | |

Overall values obtained using the RI or the CS models are in good agreement with both DFT and SMTB-Q literature results. Our values obtained for the CS model using GULP (identical to those already published [17]) are higher than the ones found by DFT except for the value of the Schottky defect. For DFT calculations, the Schottky defect corresponds to three vacancies without interaction (explaining the sole configuration in the table) which leads to a high energy of 10.7 eV. It can be noted that the SMTB-Q value of the $FP_U$ DFE is much lower than the value found with other potentials. This can be explained by the fact that no U-U interaction is implemented in the SMTB-Q formalism. As pointed out by Grimes [30], empirical potentials can be comparable to those predicted by quantum mechanical procedures but suffer from two main factors: (i) the equilibrium interatomic spacings, and (ii) the way

electronic polarisation is handled. This explains the discrepancies even if the use of the Mott-Littleton method is supposed to correct these factors. The DFE values calculated with LAMMPS (without the Mott-Littleton method) are higher. Nevertheless, the order of magnitude is respected when compared to DFT: the $FP_O$ DFE is the more stable while the FPU has a higher energy. In the following, we chose to use the Grimes RI model to investigate Cs migration processes from a qualitative point of view due to its acceptable accuracy and in order to save a lot of computation time.

### 3.3.2 Cs and U migration energies in $UO_2$ at 0K using NEB simulations

The migration of Cs and U atoms in $UO_2$ were computed using the CI-NEB method for several sets of configurations including various point defects.

Uranium dioxide has the fluorite crystalline structure with a lattice parameter equal to 5.47 Å. The fluorite structure is made of a face-centred cubic U sublattice surrounding a simple cubic O sublattice which has a periodicity of $a_0/2$. Migration paths of Cs within the fluorite structure are schematized in Figure 8.

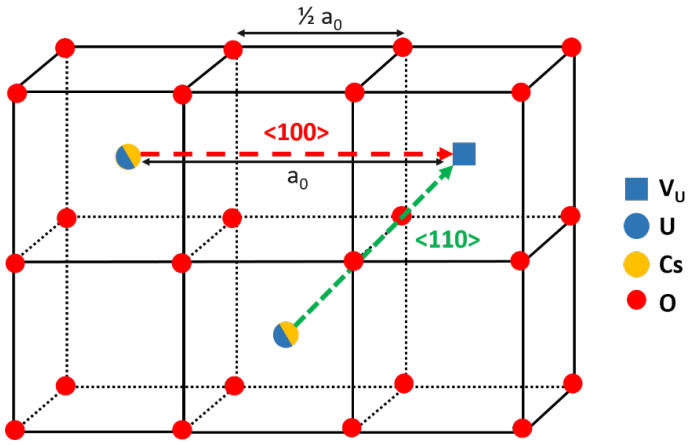


**Figure 8-** Migration paths of cesium (yellow) or uranium (blue) along the <100> (red arrow) and <110> directions (green arrow), towards a uranium vacancy (blue square) in the $UO_2$ oxygen sub-lattice (red circles).

Table 4 shows the activation energies computed for the migration of a U or Cs atom initially located into a uranium vacancy and migrating along the <100> or <110> direction as described in Figure 8 (red and green arrows). Results are compared to DFT based literature data [9]. U or Cs atom migration to a uranium vacancy is more favourable along the <110> direction than along the <100> one. While migration energies obtained using the Grimes potentials are, in most cases, slightly overestimated, they remain in qualitative agreement with DFT results except for the Cs migration along the <100> direction. It is found to be less favourable than the U migration in the <110> direction in contradiction with DFT predictions.

**Table 4-** Migration energies (eV) of Cs and U through a vacancy mechanism along directions <100> and <110> in $UO_2$

| | U | | Cs | |
|---|---|---|---|---|
| ***Direction of migration*** | ***<100>*** | ***<110>*** | ***<100>*** | ***<110>*** |
| **This work (CI-NEB) with the Grimes potential [11]** | 14.8 | 7.95 | 10.53 | 1.67 |
| **DFT (NEB) from [9]** | 8.24 | 5.60 | 4.6 | 2.7 |

CI-NEB calculations were also performed in systems containing a Cs atom and a divacancy (DV) which is a defect composed of one uranium vacancy and one oxygen vacancy. Eight configurations are possible to place the oxygen vacancy in one of the summits of the cube hosting the uranium vacancy. However, according to symmetries, only three DV configurations (DV_1, DV_2 and DV_3) are unique as illustrated in Figure 9(a). Figure 9(b) presents the energy variation as a function of the normalised distance between the initial and final states for the three configurations.

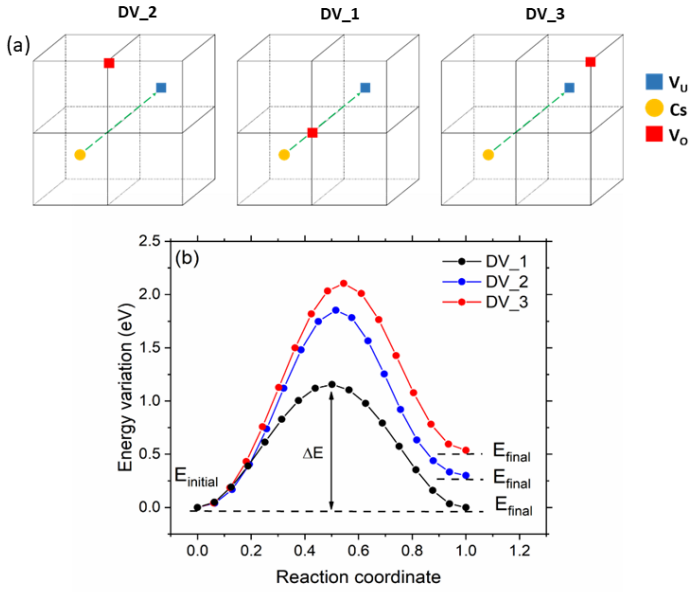


**Figure 9-** Migration of Cs towards divacancies (DV) (a) Schematic representation of the DV_1, DV_2 and DV_3 configurations in which Cs migration energies were calculated along the <110> direction. For more clarity, only the vacancies and the Cs atom are depicted in the oxygen sub-lattice (black lines). (b) Energy variation of the system as a function of the normalized distance between the NEB initial and final states.

Figure 9(b) displays a symmetric energy landscape for the DV_1 configuration with an activation energy ΔE equal to 1.15 eV. For the other configurations DV_2 and DV_3, the final energy of the system is

higher than the initial one resulting in a backward migration energy lower than in the forward case. Activation energies are presented in Table 5.

**Table 5-** Backward and forward migration energy of Cs along the direction <110> towards divacancies (DV)

| | | **DV_1** | **DV_2** | **DV_3** |
|---|---|---|---|---|
| ΔE (eV) | Backward | 1.15 | 1.55 | 1.57 |
| | Forward | 1.15 | 1.85 | 2.11 |
| *Number of equivalent configurations* | | *2* | *4* | *2* |

These results emphasize the influence of the oxygen vacancy location on the Cs migration energy. Indeed, the migration barrier decreases as the oxygen vacancy get closer to the Cs atom at the saddle point. The lower activation energy ($\Delta E$ = 1.15 eV) corresponds to the closest position of $V_O$, obtained for the DV_1 configuration. For the two other configurations, DV_2 and DV_3, as the $V_O$ gets further, the calculated energy increases up to 1.55 eV and 2.11 eV, respectively.

Finally, we determined the migration energies of a Cs atom originally located in a uranium vacancy going toward each non-equivalent configuration of a Schottky defect (S1, S2 or S3). Eleven unique Schottky configurations were determined with S3_1 being the only symmetric configuration. They are depicted in Figure 10 and the corresponding activation energies are gathered in Table 6.

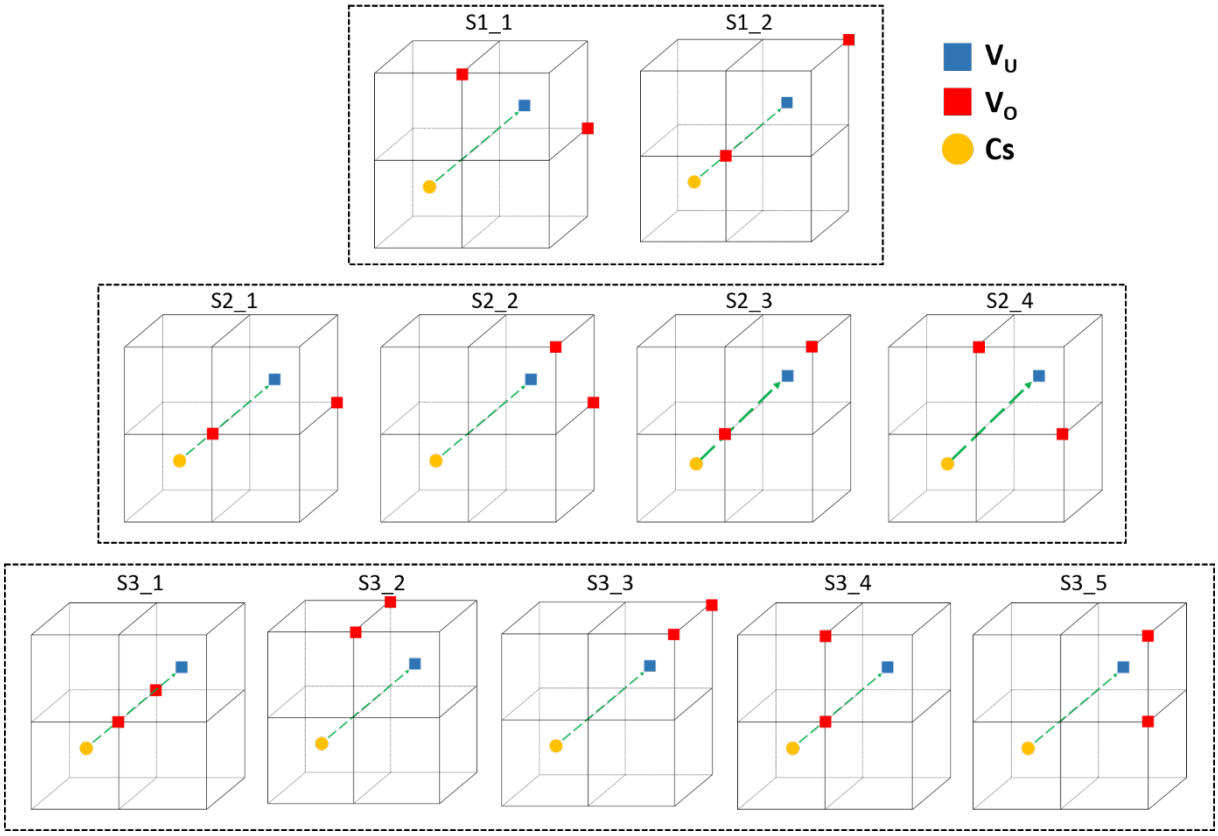


**Figure 10-** Schematic representation of the eleven different Schottky configuration considered to calculate Cs migration energies, along the <110> direction, in the uranium vacancy of a Schottky defects. For more clarity, only the vacancies and the Cs atom are depicted in the oxygen sub-lattice (black lines).

**Table 6-** Forward and backward migration energies of Cs along the direction <110> within different Schottky defect configurations in $UO_2$

| | | **S1** | | **S2** | | | | **S3** | | | | |
|---|---|---|---|---|---|---|---|---|---|---|---|---|
| | | **S1_1** | **S1_2** | **S2_1** | **S2_2** | **S2_3** | **S2_4** | **S3_1** | **S3_2** | **S3_3** | **S3_4** | **S3_5** |
| ΔE (eV) | Backward | 1.54 | 0.74 | 0.87 | 1.28 | 0.78 | 1.60 | 0.48 | 1.43 | 1.19 | 1.10 | - |
| | Forward | 2.20 | 1.33 | 1.26 | 2.15 | 1.37 | 2.23 | 0.49 | 2.16 | 2.34 | 1.50 | - |
| *Number of equivalent config.* | | *2* | *2* | *4* | *4* | *2* | *2* | *1* | *2* | *1* | *2* | *4* |

The results presented in Table 6 can be grouped within three families. The first one corresponds to configurations where the Cs atom has to go through the oxygen lattice to reach the uranium vacancy.

In this case, the Cs forward migration energy ranges between 2.15 and 2.36 eV. The second family concerns an oxygen vacancy between the Cs atom and the uranium vacancy, at a distance of $\frac{a_0}{2}\sqrt{3}$. For these configurations, the Cs forward migration energy is comprised between 1.26 and 1.50 eV. Finally, when both oxygen vacancies are close to the Cs atom (S3_1), the migration barrier is very low, with a value of 0.49 eV. We were not able to determine the Cs barrier migration of the S3_5 configuration due to the unwanted migration of one of the $V_O$, resulting in the formation of a S2_3 Schottky.

### 3.3.3 MD simulation of Cs migration at high-temperature

The same initial configurations than for the NEB calculations were chosen to run MD simulations at a temperature of 2227°C. During the runs, each atom was free to move according to local forces and thermal fluctuations. However, despite the elevated temperature, uranium atoms and $V_U$ created for each configuration were shown to remain immobile. This behaviour is attributed to the activation energy (> 7.95 eV as shown in Table 4) which is really high precluding U self-diffusion to happen in our simulation times.

As a first step, we computed the Cs MSD as a function of time for a Cs atom incorporated into a VU close to another VU along the direction <110> or along the <100> one. In total, 11 runs were performed for each direction to obtain statistically meaningful results. An example is displayed in Figure 11(a). We observe that the value of the Cs MSD oscillates between the Cs initial position (MSD = 0 Å²) and the position inside the uranium vacancy (MSD value of ~15 Å²). This confirms that a Cs atom jumps between the two uranium vacancies which are displayed on the right side of the Figure 11. From this specific simulation, we counted five Cs jumps indicated by blue arrows in Figure 11.

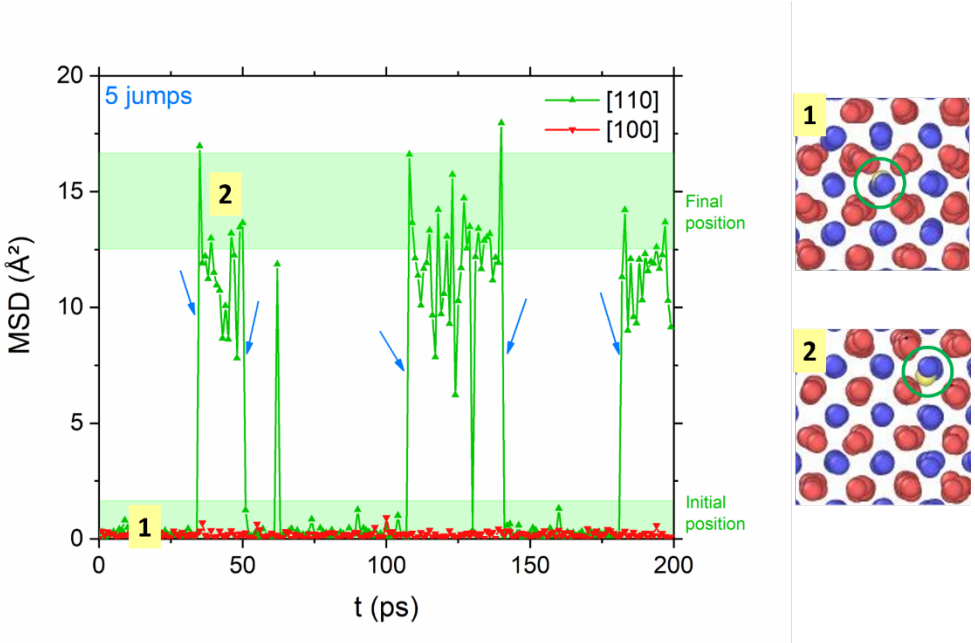

**Figure 11-** Example of a MSD evolution of Cs with time for a temperature of 2227°C. Initially, the Cs atom is placed in a $V_U$ and can diffuse in another $V_U$ along the <110> or the <100> direction (positions 1 and 2 shown on the right side). The arrows indicate the jumps of Cs in the uranium vacancy. To help the interpretation, green bands indicate the MSD values corresponding to the Cs initial position (MSD = 0 Å²) and the final position (in $V_U$) of the Cs atom for <110> direction, centred around the theoretical MSD value of ~15 Å² (the square of the distance between the Cs atom and the $V_U$ which is $\frac{a_0\sqrt{2}}{2}$)

No Cs diffusion along the <100> direction (red curve in Figure 11) was recorded which can be explained by the high corresponding energy barrier of 10.5 eV. On the contrary, an average performed on the whole eleven simulations shows 4.7 ± 3.0 Cs jumps along the <110> direction. This indicates that, even if Cs atoms are mobile in $UO_2$, the Cs diffusion is impeded by the even lower self-diffusion of U as already discussed in [9,10]. In this case, the frame-by-frame analysis of the simulations allowed us to highlight an indirect mechanism for the Cs diffusion. The intermediate state corresponds to a Cs position between two oxygen atoms, at mid-distance of the two $V_U$ (see Figure 8). This corresponds to the saddle point identified in the corresponding CI-NEB calculation. The MD simulations show two cases when the Cs atom approaches closer to this saddle point. The first one corresponds to a failed attempt, which results in a sharp peak between a MSD value decreasing from ~15 Å² down to ~7.5 Å² (Figure 11). In this case, the Cs atom goes back to its departure site. The second one relates to a successful attempt, which matches with a MSD value changing from ~15 Å² down to ~0 Å². In all our simulations, the Cs atom jump from $V_U$ to another $V_U$ implies the formation of an oxygen vacancy created from one of the two oxygen atoms located near the saddle point. The oxygen atom « kicked out » in an interstitial position can move afterwards in the lattice.

Cesium MSD was also computed in systems containing either a divacancy or a Schottky defect. Calculations were made for the three divacancy configurations (DV_1, DV_2 and DV_3) and also for the S1, S2 and S3 Schottky configurations. In our simulation conditions, oxygen vacancies become mobile around 1527°C. Thereby, as the temperature increases during the simulations, we systematically observed a rearrangement of the oxygen atoms in the DV and the Schottky defects that resulted in the symmetric configurations DV_1 and S3_1, respectively, that are the most favourable defects as previously calculated by CI-NEB. Averaging the number of Cs atomic jumps in 200 ps, for each DV simulations, leads to 4.7 ± 3.1 jumps. This value is quasi identical to the result obtained for the sole uranium vacancy configuration. This is explained by the fact that when the Cs atom goes through the saddle point, the configuration remains the same. An oxygen vacancy must be created to allow the Cs jump.

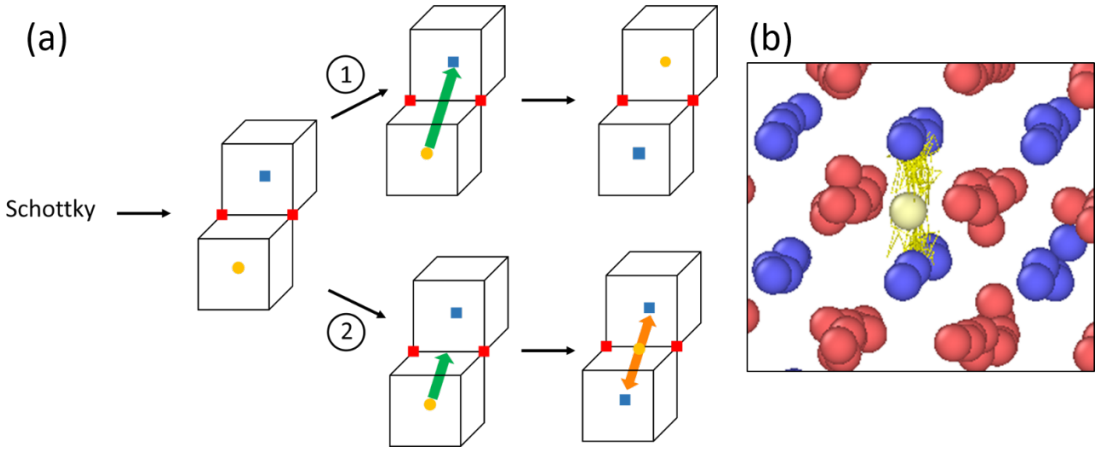


**Figure 12-** (a) Illustration of the two possible cases (namely (1) and (2) on the figure) for the Cs behavior after S3_1 formation with temperature, the Cs atom either jumps easily in the uranium vacancy or is stabilized at the center of the tetravacancy thus formed. Caption is identical to previous figures. (b) OVITO visualization of the trajectory (yellow line) of an atom of Cs (yellow) stabilized in a tetravacancy, jumping continuously between the two uranium vacancies.

For the Schottky simulations, we observed two cases. In half of the runs, the Cs atom was stabilized in the centre of the tetravacancy created by the Cs atom leaving its initial site. Then, an endless back and forth movement of the Cs atom in each uranium vacancy occurs (Figure 12 (b)). For the other half simulations, we obtained an average of 11.2 ± 1.8 jumps which agrees with the energy barrier value, the lowest of all those calculated using the CI-NEB methods.

# 4. DISCUSSION

It is quite well-known that Cs forms bubbles at low temperature. At a temperature threshold of 600°C, Sabathier *et al.* [31] highlighted the formation of 1.7 nm sized Cs bubbles in $UO_2$ implanted with cesium at a fluence of $10^{16}$ at $cm^{-2}$. Moreover, bubbles of around 1-2 nm were observed in $UO_2$ implanted with cesium at a fluence of $10^{15}$ at $cm^{-2}$ after a 1000°C annealing [16]. As long as the trapping into bubble prevails, no Cs long range diffusion can occur. This is why below 1200°C, the cesium distribution is unchanged compared to the as-implanted one in our study. Therefore, between 600°C and 1000°C, cesium migration at short range can only occur to allow Cs bubble nucleation into defects like those created by implantation. The nucleation centre of these small bubbles is most probably a defect containing at least a uranium vacancy since Cs incorporation energies into a single uranium vacancy, a divacancy and a Schottky defect are negative according to DFT calculations [9].

At 1200°C, only slight changes appear in the Cs distribution after four hours annealing. However, a remarkable evolution was observed after twelve hours with the apparition of three peaks. TEM observations were performed on this latter sample. Nanobubbles of around 1 nm in size were observed within the first 300 nm from the surface which corresponds to the presence of the implanted cesium atoms. Three regions were delimited. The first Zone corresponds roughly to the two first peaks observed by SIMS. A very rough density estimate was calculated for zone 1, yielding an order of magnitude of $10^{24}$ nanobubbles $m^{-3}$. A similar estimate could not be performed in the other zones. However, it can be qualitatively estimated that the ~1 nm sized nanobubble density is higher at the bottom of zone 1 (~60-80 nm from the surface) than in proximity of the surface. In zone 2 and zone 3, we could observe some bigger bubbles (~5 nm) and some rare faceted bubble of the same size. This means that some coalescence process has occurred at the place where a maximum of defects and Cs concentration can be found. These few bubbles show that 1200°C is really a threshold temperature to start the migration of cesium which can lead to the growth of some bubbles and the disappearance of smaller bubbles as it was observed at 1600°C in [16]. However, since the Cs peaks position observed in the SIMS profiles evolves with the annealing time, no diffusion coefficient was calculated at 1200°C. Nevertheless, these peaks may be the premises of the three contributions distinguished in the Cs distributions obtained in the 1300-1600°C temperature range. Two of them are explained by the trapping of cesium atoms into implantation defects and the last one is attributed to Cs diffusion occurring after thermal resolution process. They were respectively fitted by Gaussian distributions named G1, G3 and G2. G1 distribution accounts for cesium atoms trapped into bubbles near the surface (at ~50 nm) where most of point defects are created by the implantation process. These bubbles have grown from spherical to bigger faceted bubbles through an Ostwald mechanism as explained in ref. [16]. Faceted bubbles growth is certainly favoured by the surface proximity: the flux of vacancies brought by the surface at high temperature may form clusters of defects able to stabilize these bubbles. This is consistent with Murphy *et al.* [32] MD simulations, which have shown that xenon was particularly stable in nanovoids formed by several Schottky defects. However, the growth of these faceted bubbles seems to be limited. At 1300°C, no Cs release was observed, which means that Cs diffusion towards the surface (in the long range) is not effective due to the trapping of Cs into bubbles at ~50 nm from the surface. On the contrary, important releases were observed at 1400°C and 1600°C (35 to 50%) and the accumulation peak was significantly lower. Thus, as the temperature increases, the equilibrium between long-range diffusion and trapping mechanisms changes: above 1300°C, the diffusion process is favoured over the trapping, when maximum size and/or density of faceted bubbles is reached. G3 distribution is also attributed to a trapping of cesium atoms into implantation induced defects. At depths greater than 50 nm, TEM analysis did not show any Cs bubble [16]. As the Cs solubility limit in $UO_2$ (around ~0.01 at.% at 1700°C according to [33]) is exceeded in this second

distribution, this would suggest a competition between thermal resolution process, diffusion and trapping of the Cs atoms. Our MD simulations show that at high temperature, the Cs atoms can easily jump from a uranium vacancy to another type of defect containing a uranium vacancy, with the exception of the tetravacancy. Since there are no vacancy sources available nearby as opposed to the trapping contribution of G1, no bigger defects can form to stabilize the Cs bubbles. We thus hypothesise that only small clusters of cesium and vacancies are created limiting thereafter the Cs diffusion. Finally, the G2 distribution corresponds to Cs diffusion towards the bulk material, in a region where the Cs concentration is around the solubility limit. This region is free from point defects but contains some dislocation loops created by the implantation collision cascades [16]. To further understand the effect of defects on the Cs migration in $UO_2$, some activation energies found in the literature for different conditions of irradiation and temperature are reported in Table 7.

**Table 7-** Comparison of the pre-exponential factors ($D_0$) and activation energies (Ea) of Cs diffusion in $UO_2$ fuel available in the literature compared to our value (bold)

| Sample history | T (°C) | Do ($cm^2\ s^{-1}$) | Ea (eV) | Ref. |
|---|---|---|---|---|
| Post-irradiation annealing BU: 47 GW.d.$t_U^{-1}$ | 1500 - 2500 | $2.1\ 10^{-8}$ | 1.6 | [34] |
| **$UO_2$ implanted with at $10^{15}$ at $cm^{-2}$ and annealed** | **1300 - 1600** | **$5.6\ 10^{-9}$** | **1.8** | **This work** |
| Post-irradiation annealing 38 < BU < 44 GW.d.$t_U^{-1}$ | 1200 - 2200 | $7.6\ 10^{-3}$ | 3.2 | [35] |
| Post-irradiation annealing 10 < BU < 30 GW.d.$t_U^{-1}$ | 1200 - 2200 | $2.0\ 10^{-3}$ | 4.2 | [35] |
| Post-irradiation annealing Slightly irradiated $UO_2$ (~1 ppb of Cs) | 1450 - 1750 | $3.4\ 10^{-2}$ | 4.3 | [8] |

Table 7 displays a wide range of activation energies values, from 1.6 eV to 4.3 eV, which implies different Cs migration mechanisms (assuming no deviation of the stoichiometry). First, we will consider the experiment of Prussin et al. with only 1 ppb of cesium in a very slightly irradiated $UO_2$ sample [8]. Almost no irradiation induced defects are produced. The formation of uranium vacancies is only activated by the temperature (between 1450 and 1750°C) during each annealing. Therefore, only a small fraction of vacancies is available for Cs diffusion and the uranium diffusion is the limiting process. This corresponds to our MD simulations where no jumping of uranium atoms occurred, preventing Cs from diffusing, despite its ability to jump between uranium vacancies. The activation energy calculated by DFT for the diffusion of a uranium atom towards an uranium vacancy is 5.6 eV [9]. This value is close, even if slightly higher, to the one found by Prussin *et al.* (4.3 eV) [8] and the one found by

568 Osborne *et al.* (4.2 eV) [35] for irradiation experiments done at low burnup (maximum value of
569 30 GW.d.tU$^{-1}$).
570 On the contrary, Kudo *et al.* [34] measured a low activation energy of 1.6 eV in a highly damaged $UO_2$
571 sample indicating that uranium diffusion is no more the limiting step for the Cs diffusion because of
572 the presence of a high concentration of defects. Similarly, we obtained a low value (1.8 eV) because of
573 the annealing of extended defects created during the implantation process, thus creating a flux of point
574 defects, especially vacancies enhancing the Cs diffusion.
575 Besides, our MD simulations outline the role of oxygen atoms on Cs diffusion in $UO_2$, which can be
576 considered as a Cs diffusion mechanism assisted by oxygen vacancies. Indeed, MSD calculations always
577 resulted in an oxygen migration enhanced by the presence of the cesium atom, independently of the
578 initial configuration. Considering the particular case of the Schottky defect, regardless of the initial
579 Schottky type, it invariably results in the symmetric configuration (S3_1) where the two oxygen
580 vacancies are between the Cs atom and the $V_U$. If the Cs atom (initially in $V_U$) migrates at the centre of
581 the defect, it forms a tetravacancy, where it can be stabilised. However, CI-NEB calculation in this
582 configuration resulted in a particularly low value for Cs internal migration (~0.5 eV). Thus, if we
583 consider formation of others vacancies close to the tetravacancy, this could lead to an enhanced
584 diffusion process. Then, the Cs atomic diffusion would only rely on oxygen vacancy diffusion between
585 the different uranium vacancies.
586 Concerning divacancies, they behave similarly to the Schottky defects, ending up each time in the
587 symmetric configurations (DV_1). For initial configurations where there is only one $V_U$ in the system,
588 an oxygen vacancy is created by oxygen migration following the Cs atom attempts to jump as
589 illustrated in Figure 13. Hence, the most probable migration path for the Cs atom seems to be through
590 a sole oxygen vacancy. The corresponding barrier migration energy calculated by CI-NEB is around
591 1.2 eV, which is of the same order of magnitude than in our experiment. Of course, the Grimes
592 interatomic potentials have been found to underestimate the Cs diffusion into $V_U$ in comparison with
593 the DFT value. However, this mechanism with the oxygen vacancy should have a lower activation
594 energy in DFT than the one with only the uranium vacancy which would be closer to the values found
595 by the different experiments.

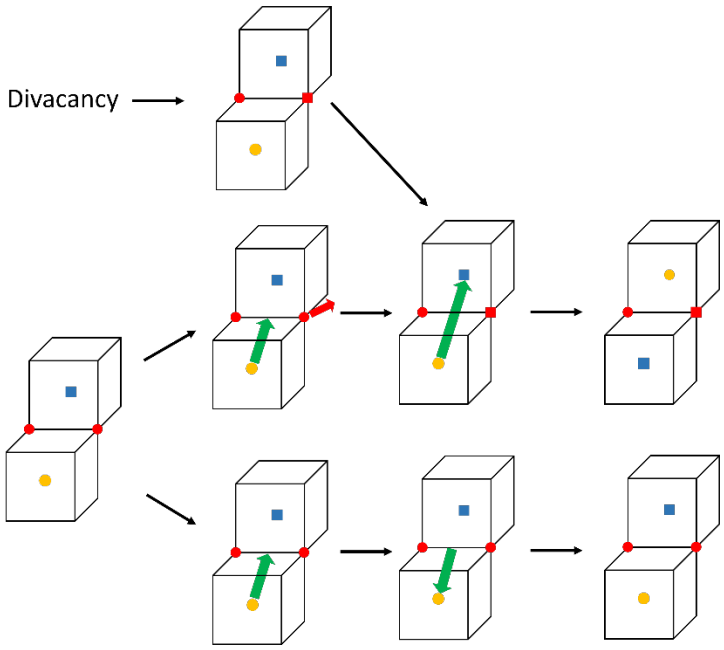


**Figure 13-** Illustration of the Cs migration assisted by one oxygen vacancy between two uranium vacancies in direction <110>. For initial configuration without a $V_O$ initially present, the Cs jump requires that an oxygen atom leave, otherwise the attempt to reach the $V_U$ fail. Caption is identical to previous figures

Finally, to be able to observe (by MD simulations) Cs diffusion through the $UO_2$ crystal, several uranium vacancies should be initially placed in the system to allow the Cs atom to diffuse through this predefined path. Such calculations are not advised, as they would generate too many additional charges in a system that is rather small (1500 atoms) in the first place. Another solution would be to develop Cs interactions with U and O with a potential such as the SMTB-Q potential that is already available to efficiently describe U and O interactions in an effective manner [27,36,37].

# 5. CONCLUSION

The aim of this paper was to investigate the Cs migration in $UO_2$ to obtain a better understanding of its behaviour in the fuel, especially under accidental conditions at high temperature. SIMS experiments highlighted the complex behaviour of cesium between 1000°C and 1600°C. This behaviour is the consequence of the competition between several mechanisms, each one prevailing at different temperatures. At relatively “low” temperatures up to 1000°C, Cs mainly forms nanometric bubbles which results in no apparent diffusion within the timescale of the laboratory. 1200°C seems to be a threshold temperature at which the motion of the cesium atoms and the subsequent untrapping process occur. This mainly indicates a thermal resolution mechanism which allows Cs atoms to migrate at short distances. Between 1300°C and 1600°C, Cs bubbles exist only in a very limited zone near the

surface. Elsewhere, thermal resolution prevails allowing Cs atoms to diffuse. We established a model to estimate apparent Cs diffusion coefficients from the depth profiles and we determined an activation energy of 1.8 eV which is one of the smallest compared to the literature data. The atomistic simulations show that this low value is due to the Cs atoms jumping towards defects containing a uranium vacancy without being limited by the uranium diffusion. This is the case in our experiments, where high concentration of vacancies is created by the annealing of the extended defects (mainly interstitial dislocation loops) formed during the implantation process. The combination of CI-NEB and MD simulations show that the most probable process to explain Cs atomic diffusion is through a U-O divacancy. Two configurations were identified at the saddle point. If an oxygen vacancy exists, the cesium atom can go through it freely. Otherwise, an oxygen vacancy is always created before allowing the Cs migration.

## Acknowledgements

The authors thank Anthony Duranti (IP2I Lyon, France) for the Cs implantation at the IMIO400 implanter, Dr. Philippe Sainsot for interferometry measurements (INSA Lyon. France) and M. Mommey and Y. Giraud (IP2I Lyon, France) for their help with the HPC.

## AIP Publishing data sharing policy

The data that support the findings of this study are available from the corresponding author upon reasonable request.

# References


[1] D. Champion, I. Korsakissok, D. Didier, A. Mathieu, D. Quélo, J. Groell, E. Quentric, M. Tombette, J.P. Benoit, O. Saunier, V. Parache, M. Simon-Cornu, M.A. Gonze, P. Renaud, B. Cessac, E. Navarro, A.C. Servant-Perrier, Radioprotection 48, 11 (2013). doi:10.1051/radiopro/2012052.

[2] G. Ducros, P.P. Malgouyres, M. Kissane, D. Boulaud, M. Durin, Nucl. Eng. Des. 208, 191 (2001). doi:10.1016/S0029-5493(01)00376-4.

[3] Y. Pontillon, G. Ducros, Nucl. Eng. Des. 240, 1867 (2010). doi:10.1016/j.nucengdes.2009.06.028.

[4] A. Hidaka, T. Kudo, T. Nakamura, H. Uetsuka, J. Nucl. Sci. Technol. 39, 273 (2002). doi:10.1080/18811248.2002.9715185.

[5] T. Kudo, M. Kida, T. Nakamura, F. Nagase, T. Fuketa, J. Nucl. Sci. Technol. 44, 1421 (2007). doi:10.1080/18811248.2007.9711389.

[6] Y. Pontillon, E. Geiger, C. Le Gall, S. Bernard, A. Gallais-During, P.P. Malgouyres, E. Hanus, G. Ducros, J. Nucl. Mater. 495, 363 (2017). doi:10.1016/j.jnucmat.2017.08.021.

[7] A.H. Booth, A method of calculating fission gas diffusion from UO2 fuel and its application to the X-2-f loop test, 1957.

[8] S.G. Prussin, D.R. Olander, W.K. Lau, L. Hansson, J. Nucl. Mater. 154, 25 (1988). doi:10.1016/0022-3115(88)90115-8.

[9] F. Gupta, A. Pasturel, G. Brillant, J. Nucl. Mater. 385, 368 (2009). doi:10.1016/j.jnucmat.2008.12.009.

[10] G. Busker, R.W. Grimes, M.R. Bradford, J. Nucl. Mater. 279, 46 (2000). doi:10.1016/S0022-3115(99)00274-3.

[11] R.W. Grimes, C.R.A. Catlow, Philos. Trans. R. Soc. London. Ser. A Phys. Eng. Sci. 335, 609 (1991). doi:10.1098/rsta.1991.0062.

[12] J.P. Crocombette, J. Nucl. Mater. 305, 29 (2002). doi:10.1016/S0022-3115(02)00907-8.

[13] G. Brillant, F. Gupta, A. Pasturel, J. Phys. Condens. Matter. 21, 285602 (2009). doi:10.1088/0953-8984/21/28/285602.

[14] J.F. Ziegler, U. Littmark, J.P. Biersack, Stopping and ranges of ions in matter, Pergamon Press, New York, 1985.

[15] J. Soullard, J. Nucl. Mater. 135, 190 (1985). doi:10.1016/0022-3115(85)90077-7.

[16] C. Panetier, Y. Pipon, C. Gaillard, N. Moncoffre, T. Wiss, D. Mangin, O. Dieste, B. Marchand, R. Ducher, R. Dubourg, T. Epicier, L. Raimbault, J. Nucl. Mater. 543, 152520 (2021). doi:10.1016/j.jnucmat.2020.152520.

673 [17] K. Govers, S. Lemehov, M. Hou, M. Verwerft, J. Nucl. Mater. 366, 161 (2007).
674 doi:10.1016/j.jnucmat.2006.12.070.
675 [18] P.P. Ewald, Ann. Phys. 369, 253 (1921). doi:10.1002/andp.19213690304.
676 [19] S. Plimpton, Fast Parallel Algorithms for Short-Range Molecular Dynamics, J. Comput. Phys.
677 117, 1 (1995).
678 [20] J.D. Gale, A.L. Rohl, Mol. Simul. 29, 291 (2003).
679 [21] G. Henkelman, B.P. Uberuaga, H. Jónsson, J. Chem. Phys. 113, 9901 (2000).
680 doi:10.1063/1.1329672.
681 [22] E. Bitzek, P. Koskinen, F. Gähler, M. Moseler, P. Gumbsch, Phys. Rev. Lett. 97, 1 (2006).
682 doi:10.1103/PhysRevLett.97.170201.
683 [23] J. Guénolé, W.G. Nöhring, A. Vaid, F. Houllé, Z. Xie, A. Prakash, E. Bitzek, Comput. Mater. Sci.
684 175, 109584 (2020). doi:10.1016/j.commatsci.2020.109584.
685 [24] W.H. Hocking, R.A. Verrall, I.J. Muir, J. Nucl. Mater. 294, 45 (2001). doi:10.1016/S0022-
686 3115(01)00447-0.
687 [25] C. Onofri, C. Sabathier, G. Carlot, D. Drouan, C. Bachelet, C. Baumier, M. gérardin, M. Bricout,
688 Nucl. Instrum. Meth. B 463, 76 (2020). doi: 10.1016/j.nimb.2019.11.031
689 [26] L-F. He, M. Gupta, C. A. Yablinsky, J. Gan, M. A. Kirk, X.-M. Bai, J. Pakarinen, T. R. Allen, J. Nucl.
690 Mater. 443, 71 (2013). doi: 10.1016/j.jnucmat.2013.06.050
691 [27] B. Dorado, D.A. Andersson, C.R. Stanek, M. Bertolus, B.P. Uberuaga, G. Martin, M. Freyss, P.
692 Garcia, Phys. Rev. B - Condens. Matter Mater. Phys. 86, 1 (2012). doi:10.1103/PhysRevB.86.035110.
693 [28] B. Dorado, M. Freyss, B. Amadon, M. Bertolus, G. Jomard, P. Garcia, J. Phys. Condens. Matter.
694 25, 333201 (2013). doi:10.1088/0953-8984/25/33/333201.
695 [29] G. Sattonnay, R. Tétot, Bulk, J. Phys. Condens. Matter. 25, 125403 (2013). doi:10.1088/0953-
696 8984/25/12/125403.
697 [30] R.W. Grimes, C.R.A. Catlow, A.M. Stoneham, J. Phys. Condens. Matter. 1, 7367 (1989).
698 doi:10.1088/0953-8984/1/40/011.
699 [31] C. Sabathier, L. Vincent, P. Garcia, F. Garrido, G. Carlot, L. Thome, P. Martin, C. Valot, Nucl.
700 Instrum. Meth. B 266, 3027 (2008). doi:10.1016/j.nimb.2008.03.158.
701 [32] S.T. Murphy, A. Chartier, L. Van Brutzel, J.P. Crocombette, Phys. Rev. B - Condens. Matter
702 Mater. Phys. 85, 1 (2012). doi:10.1103/PhysRevB.85.144102.
703 [33] C.T. Walker, C. Bagger, M. Mogensen, J. Nucl. Mater. 240, 32 (1996). doi:10.1016/S0022-
704 3115(96)00477-1.
705 [34] T. Kudo, M. Kida, T. Nakamura, F. Nagase, T. Fuketa, J. Nucl. Sci. Technol. 44, 1428 (2007).
706 doi:10.3327/jnst.44.1428.

[35] M. Osborne, R.A. Lorenz, ORNL studies of fission product release under LWR severe accident conditions, Nucl. Saf. 33 (1992).

[36] D. MBongo, R. Tetot, R. Ducher, R. Dubourg, N. Salles, J. Phys. Condens. Matter. 32, 095701 (2019).

[37] A. Soulié, E. Clouet, F. Garrido, J.-P. Crocombette, A. Kraych, G. Sattonnay, Acta Mater. 150, 248 (2018). doi:10.1016/j.actamat.2018.03.024.